Biophysical Journal Volume 109 December 2015 2218–2226

Article

Fractal Characterization of Chromatin Decompaction in Live Cells

Ji Yi,[1,2] Yolanda Stypula-Cyrus,[1] Catherine S. Blaha,[1] Hemant K. Roy,[2] and Vadim Backman[1,*]
[1]Department of Biomedical Engineering, Northwestern University, Evanston, Illinois; and [2]Boston Medical Center, Department of Medicine, Boston University, Boston, Massachusetts

ABSTRACT Chromatin organization has a fundamental impact on the whole spectrum of genomic functions. Quantitative characterization of the chromatin structure, particularly at submicron length scales where chromatin fractal globules are formed, is critical to understanding this structure-function relationship. Such analysis is currently challenging due to the diffraction-limited resolution of conventional light microscopy. We herein present an optical approach termed inverse spectroscopic optical coherence tomography to characterize the mass density fractality of chromatin, and we apply the technique to observe chromatin decompaction in live cells. The technique makes it possible for the first time, to our knowledge, to sense intracellular morphology with length-scale sensitivity from ~30 to 450 nm, thus primarily probing the higher-order chromatin structure, without resolving the actual structures. We used chromatin decompaction due to inhibition of histone deacytelases and measured the subsequent changes in the fractal dimension of the intracellular structure. The results were confirmed by transmission electron microscopy and confocal fluorescence microscopy.

INTRODUCTION

The organization of chromatin requires the compaction of over a meter of genetic material within the limited volume of the nucleus. Consequently, chromatin compaction impacts all processes requiring physical access to the DNA sequence, such as gene transcription (1,2), DNA replication (3), and repair (4). The primary unit of chromatin is the nucleosome, which is composed of DNA wrapping around histones in a structure resembling beads on a string of DNA observed in vitro. This chromatin string further compacts into chromatin higher-order structures following a hierarchical model (5-7). The entire chromatin organization spans across at least two orders of magnitude of length scale from ~30 nm (size of chromatin fiber observed in vitro) to several microns (size of the nucleus). Surprisingly, very little is known of how chromatin is compacted and organized in live cells, particularly at length scales below the Abbe diffraction limits where higher-order chromatin organizations such as fractal globules are formed (8,9). Now, even the structure of the secondary chromatin compaction (i.e., chromatin fiber) is not entirely clear (10-13). Recent discovery states that the chromatin fiber is composed of heterogeneous groups of nucleosome clusters instead of a compacted nucleosome helix structure (14). Given the pivotal role of the higher-order chromatin structures in the broad spectrum of genome functions, it is critically important to characterize the chromatin compaction in the submicron, subdiffractional regime.

There are emerging reports suggesting that chromatin is organized in a fractal fashion, more evidently in the range of length scales from ~0.4 to 1 μm (15). Fractals exhibit self-similar structures, i.e., a characteristic structural detail can be observed at any length scale. A more rigorous definition of a fractal can be stated through the power-law spatial autocorrelation function $r^{(D-3)}$ of a particular quantity, where r is the spatial length and $D < 3$ (unitless) defines the fractal dimension (15,16). To measure structure, the most direct quantity is the mass density, whose autocorrelation functional form is defined by the mass-density fractal dimension, D_m. As a means of measuring D_m, neutron scattering is probably the most accurate method (17,18). It is reported in fixed nuclei that the fractal dimension is ~2.9 from 0.5 to 5 μm and ~2.4 from 60 nm to 0.5 μm (17). Chromosome conformation capture techniques (Hi-C) have also determined a power-law relation between the chromatin contact probability and DNA basepairs, indicating a mass density fractal distribution (8). Translating the basepairs into physical distance (19), the fractal dimension is close to 3 within the range of length scale from ~0.5 to 1 μm. Optical imaging-based methods such as texture analysis and rheology have also characterized such a power-law autocorrelation function with the fractal dimension ~2–3 in the cell nucleus (20,21). However, the inherent diffraction limit only permits resolving of structural features >0.4 μm. Angle-resolved low-coherence interferometry (a/LCI) calculated the mass fractal dimension from live cells as 1.6–2.0 at a broad length-scale range from 1 μm to 30 μm (22,23). In the literature, the data reported on characterizing chromatin compaction in the length scale below 0.3 μm are sparse, particularly in live cells where structural integrity is maintained (15).

Submitted May 1, 2015, and accepted for publication October 8, 2015.

*Correspondence: v-backman@northwestern.edu

Ji Yi and Yolanda Stypula-Cyrus contributed equally to this work.

Editor: Jochen Guck.

0006-3495/15/12/2218/9

http://dx.doi.org/10.1016/j.bpj.2015.10.014

Being able to perform measurements in live cells, optical spectroscopy can be an excellent alternative for characterization of chromatin compaction at length scales beyond the resolution limit (<0.5 μm) (24,25). Indeed, it has been demonstrated that optical spectroscopic analysis is able to detect nanoscale structural alterations (26,27). We previously developed a technique termed inverse spectroscopic optical coherence tomography (ISOCT), which uses coherence gating to obtain backscattering power spectral density from local three-dimensional (3D) tissue volume on the order of 2×10^3 μm^3 (i.e., ~$12 \times 12 \times 15$ μm in the x, y, and z dimensions) (28-30). By measuring the power-law spectral dependence, the fractal dimension of the refractive index (RI) correlation function can be indirectly recovered. Given the linear relationship between RI and macromolecular mass density, ISOCT is then able to quantify D (31,32). The unique advantage of ISOCT is that the measurement of D is sensitive to structural alterations at length scales from ~30 nm to ~450 nm, beyond the resolution limit of conventional OCT (28).

Here, we used ISOCT to quantify the fractality of live cells undergoing chromatin remodeling. Chromatin compaction is partly mediated by histone deacetylases (HDACs), a class of enzyme that allows DNA to wrap around histones. We inhibited the HDACs using valproic acid (VPA) to decompact the overall chromatin structure and determine changes in fractality (33,34). Furthermore, we used high-resolution transmission electron microscopy (TEM) imaging and confocal fluorescence microscopy of the nuclei to visualize and determine the effect of chromatin decompaction in fixed cells. Finally, the progression of chromatin decompaction in live cells is observed and quantified over time. Using multiple techniques, we consistently observed a reduced fractal dimension, D, upon treatment with VPA, suggesting a sharper mass-density autocorrelation function at subdiffractional regime (i.e., the autocorrelation function decays faster at longer spatial length).

This article is organized as follows. The Materials and Methods section describes the experimental and data-processing methods. The Results section will introduce the theory and explain the experimental results. The Discussion and Conclusion sections will discuss the implication of this study and conclude the article.

MATERIALS AND METHODS

Cell culture and treatment

Human colon cancer HT-29 cells were grown in McCoy's 5A medium (ATCC, Manassas, VA) supplemented with 10% fetal bovine serum and 50 mg/mL penicillin/streptomycin in a 5% CO_2 environment at 37°C. The C-terminus Src kinase (CSK) shRNA stably transfected HT-29 cells were selected as a clonal population and grown as previously reported (35). CSK is a key tumor suppressor in colorectal cancer, where knockdown in HT-29 cells leads to increased aggressiveness and alterations in optical properties (35-38). For pharmacological inhibition of HDACs, increasing concentrations of VPA (Sigma-Aldrich, St. Louis, MO) were applied to cells based on previous results (33,39). Concentrations tested ranged from 0.1 mM to 1.5 mM and cells were treated for 1, 2, 4, 6, and 24 h before cell-viability and ISOCT measurements.

WST-1 cell viability assay

CSK knockdown HT-29 cells were incubated in normal conditions for 48 h in 96-well plates. After VPA treatment, 4-{3-(4-iodophenyl)-2-(4-nitrophenyl)-2H-5-tetrazolio}-1, 3-benzene disufonate reagent (WST-1) (Roche Diagnostics, Indianapolis, IN) was added to the plates for cell-viability detection. After 45 min incubation with WST, the absorbance of the plate was read at 440 nm and 600 nm using a Spectramax Plus spectrophotometer plate reader (Molecular Devices, Sunnyvale, CA).

Confocal microscopy and histogram analysis

Approximately 50,000 cells were grown overnight on glass coverslips. Cells were then fixed in 4% paraformaldehyde for 20 min on ice and washed twice with Dulbecco's phosphate-buffered saline (PBS) (ATCC) for 5 min each. Next, cells were permeabilized using 0.1% Triton X-100 in PBS for 20 min at room temperature. Then, 1% bovine serum albumin in PBS was applied for blocking for 20 min. Chromatin staining was carried out using TOPRO3 (Invitrogen, Carlsbad, CA) for 15 min. Finally, the coverslips were mounted in ProLong Gold antifade reagent (Invitrogen) onto glass slides. Specimens were imaged using a confocal microscope (Leica SP5 with Leica Systems software, Wetzlar, Germany). For the image analysis, intensity histograms were generated using ImageJ (NIH, Bethesda, MD). Intensity histograms were normalized to the pixel count for each nucleus and the standard deviation of the resultant intensity was calculated in Microsoft Excel.

Transmission electron microscopy preparation and image analysis

Cells were treated with 0.5 mM VPA for 24 h. Cell pellets were collected by centrifugation at 900 rpm. The cell pellets were then immediately frozen at high pressure using a Leica EM-PACT2 high-pressure freezer at the Biological Imaging Facility of Northwestern University. Next, automatic freeze substitution was carried out using a Leica AFS2 system. The cell samples were embedded in Epon 812 resin (Electron Microscopy Sciences, Hatfield, PA) and finally thin-sectioned into 90 nm sections onto copper grids using a Leica Ultracut S microtome. High-resolution digital images of samples were collected using a JEOL 1230 (Tokyo, Japan) and Advanced Microscopy Techniques (Woburn, MA) imaging software.

To calculate the fractal dimensions, D_{TEM}, of the TEM image-correlation function on cell nuclei and whole cells, we first manually lineated the nuclear periphery and selected only the nuclear images. Then, we manually lineated the cell periphery to include the whole cell. In the case where some parts of a cell were outside the field of view, we used the image boundary as the periphery. The mean value of the nuclear region or a whole cell was subtracted and a 2D Fourier transform was performed to obtain the reciprocal image in the Fourier domain. Based on the Wiener-Khinchin theorem, we squared the absolute values of the reciprocal image in the frequency domain and performed a 2D inverse Fourier transform to yield the 2D correlation map. The final correlation function was obtained by a radial averaging on the 2D correlation map around the origin. The image correlation function, $C_r(r_d)$, was then fitted by a power-law equation:

$$C_r(r_d) = a \times r_d^{D_{TEM}-3}, \tag{1}$$

where r_d (μm) is the spatial displacement, a is constant, depending on the magnitude of the image intensity fluctuation, and D_{TEM} is the fractal dimension calculated from TEM images.

ISOCT instrumentation and data processing

The setup of the OCT instrumentation has been described in detail previously (29). Briefly, a free-space Fourier-domain OCT (FDOCT) configuration was adopted with an illumination wavelength ranging from 650 to 800 nm, as illustrated in Fig. 1 *A*. A cube beamsplitter was used to create a Michelson interferometer and the light was focused on the sample by an objective lens. A two-dimensional galvanometer was used to steer the beam over the sample to obtain transverse discrimination. A 2048-pixel line-scanning camera was used to acquire the interference spectrum. The axial and transversal resolution were estimated at 1.5 and 12 μm, respectively. A raster scanning protocol was implemented to acquire signals. An area of 2 mm^2 was scanned at 256 × 256 pixels transversally. The exposure time was 300 μs, yielding the total acquisition time of ~25 s.

To calculate *D*, the following data processing was performed. The raw spectrum was first preprocessed by normalization of the source spectrum, subtraction of the DC components, and resampling with an equal wavenumber interval. Then, a short-time inverse Fourier transform with a sweeping Gaussian window was performed to obtain a series of wavelength-dependent 3D images, as in Fig. 1 *B*. The full width at half-maximum of the Gaussian window was $k_w = 0.36\ \mu\text{m}^{-1}$. After applying short-time inverse Fourier transform, the axial resolution was relaxed to ~15 μm. The intensity from the top 200 μm of each cell pellet was averaged to yield a spectral profile, *I*(*k*). A power-law function was used to fit the spectra with the exponent equal to $2 - D/2$ (Fig. 1 *C*) (29):

$$I(k) \sim k^{2-D/2}, \tag{2}$$

where *k* is the wavenumber, $k = 2\pi/\lambda$.

RESULTS

Optical measurement of mass-density fractal dimension *D*

The fundamental building blocks of living cells are macromolecules. Based on the Gladstone-Dale equation, tissue RI is proportional to the local macromolecular mass density (31,32):

$$n = n_0 + \rho\alpha, \tag{3}$$

where ρ (g/mL) is the local mass density of the solid material (e.g., macromolecules) and α is the RI increment, usually equal to 0.17 mL/g for biological materials. n_0 is the RI of water. The heterogeneous distribution of mass density creates fluctuation of RI and leads to elastic optical scattering.

Because of the heterogeneous nature of the mass-density distribution, we modeled tissue as a random medium with mass density continuously fluctuating. The most comprehensive way to describe such a medium is by its correlation function, i.e., the mass-density correlation function (40-42). We used a three-parameter functional family, the Whittle-Matérn (WM) function, to quantify the function form (43). This versatile functional family covers essentially all the commonly used correlation functions, including the power-law function, the Booker-Gordon formula (exponential correlation), the Gaussian model, and the Kolmogorov spectrum (von Kármán spectrum). The WM functional family is formulated as

$$B_n(r_d) = A_n\left(\frac{r_d}{L_n}\right)^{(D-3)/2} K_{(D-3)/2}\left(\frac{r_d}{L_n}\right), \tag{4}$$

where $K_{\{.\}}$ is a modified Bessel function of the second type; A_n is the amplitude of the RI fluctuation; *D* is the functional shape factor determining the type of the function; and L_n is the length scale of the correlation function whose exact meaning depends on *D* (24,30). Examples of different functional shapes under different *D* are plotted in Fig. 1 *D*. When $0 < D < 3$, the correlation function has the form of a power law and the tissue is organized as a fractal. Given the linear relationship between RI and mass density, *D* is the mass-

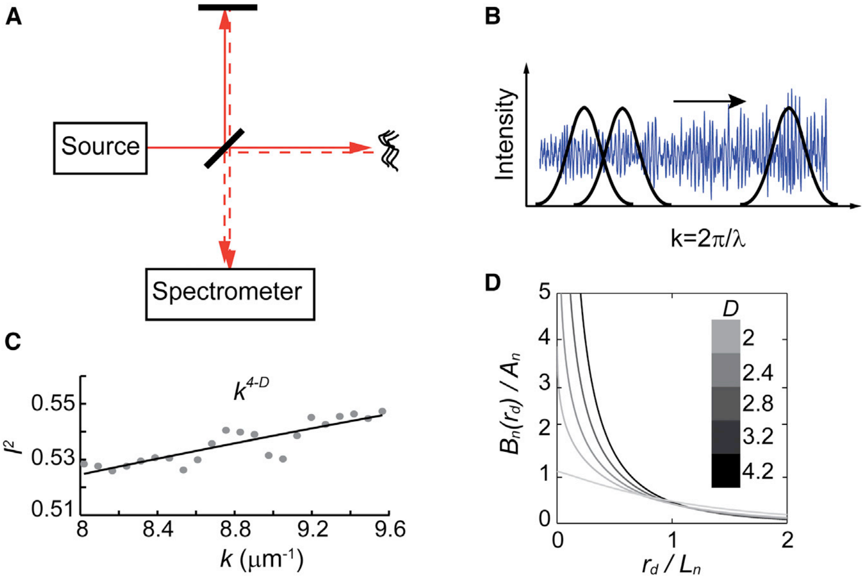

FIGURE 1 Principle of ISOCT. (*A*) A Michelson interferometry with a low temporal coherence source was used to coherently gate the backscattered light from different depths. (*B*) A short-time Fourier transform was used to obtain local spectral profiles by sweeping a Gaussian spectral window through the interferogram. (*C*) *D* was calculated by fitting the local spectra with a power-law function. (*D*) Examples of WM correlation functions at different *D* values, which established the power-law behavior of the backscattering spectrum. To see this figure in color, go online.

density fractal dimension, D_m. When $3 < D < 4$, the functional form is a stretched exponential. For $D = 4$, $B_n\ (r_d)$ is an exponential function, where $B_n\ (L_n) = B_n\ (0)\ e^{-1}$. When D approaches infinity, the function turns into a Gaussian form.

With ISOCT, the coherent gating from the interferometry allows us to interrogate a microscopic volume on the order of 10 μm^3; thus, the first-order Born approximation can be applied to predict the scattering power spectral density, Φ, by the Fourier transform of $B_n(r_d)$, $\Phi(k) = FT(B_n)$ (43). Then, the differential cross section per unit volume, $\sigma(\theta, \phi)$, can be analytically expressed, where θ and ϕ denote the scattering angle in a spherical coordinate. Since OCT detects the backscattered light, the light intensity is proportional to the backscattering coefficient, μ_b (30). The conditioned function of μ_b is

$$\mu_b = A_n 2^{\left(\frac{D}{2}+\frac{1}{2}\right)} \pi^{\frac{3}{2}} \Gamma\left(\frac{D}{2}\right) L_n^{3-D} k^{4-D}, \qquad kL_n \gg 1 \qquad (5)$$

where Γ is the gamma function. The backscattering spectrum is a power-law function to k, where the exponent is equal to $4 - D$.

OCT uses a low-coherence light source covering a wide optical bandwidth. The spectral information inherently is contained in the interferogram. By using a time-frequency analysis such as short-time inverse Fourier transform, the spectrum from each spatial voxel can be extracted. The OCT intensity at the surface is approximated as (30)

$$I^2(k) = I_0^2 r \mu_b(k) L \sim k^{4-D}, \qquad (6)$$

where I_0 is the illumination intensity, r is the reflectance on the reference arm, and L is the temporal coherence length of the source. Then, a power-law function of k is fitted to obtain the exponent and the mass fractal dimension, D.

Chromatin decompaction induced by VPA: microscopy cross validation

To observe the effect of chromatin decompaction, we acquired TEM images of cell nuclei treated with the HDAC inhibitor VPA. Following standard TEM sample processing with OsO_4, the distribution of heterochromatin and euchromatin can be distinctly identified, as in Fig. 2 *A*. We calculated and compared the image-correlation functions of nuclei from control (untreated) and 0.5-mM-VPA-treated CSK shRNA knockdown HT-29 cells, as plotted in Fig. 2 *B*. The correlation function over the range 20 nm to 0.1 μm decays faster with increasing r_d, indicating more fine structures of relaxed chromatin. We calculated the fractal dimension, D_{TEM}, based on the image correlation function, and VPA-treated cells exhibited lower D_{TEM} (Fig. 2 *C*). Importantly, D_{TEM} calculated from whole cells was also lower in VPA-treated cells than in controls, which indicates that the relaxation of chromatin in nuclei was a major contributor to the whole-cell D_{TEM} changes. Note that D_{TEM} calculated from TEM images is not exactly equal to the actual mass-density fractal dimension, because the staining does not represent the true value of mass density but rather the chemical affinity of the OsO_4. Nonetheless, we can use TEM analysis here as a qualitative confirmation of chromatin decompaction at nanometer scales.

Next, we confirmed the dose-dependent chromatin decompaction caused by VPA. Chromatin was stained with TOPRO3 and visualized using confocal fluorescence microscopy (Fig. 2 *D*). The chromatin heterogeneity was measured by calculating the standard deviation of the fluorescence-intensity distribution (Fig. 2 *E*). A large deviation of the intensity indicated a more compacted chromatin, whereas a smaller deviation denotes a less compacted chromatin structure. Fig. 2, *D* and *E*, shows a typical nucleus image and its corresponding intensity histogram of fluorescence, respectively. We observed progressive chromatin decompaction with increasing VPA concentration, as shown in Fig. 2 *F*. Together, the TEM and confocal results confirmed chromatin decompaction upon treatment with VPA.

ISOCT image of chromatin decompaction in live cells

Although confocal microscopy analysis of DNA distribution showed differences in chromatin structure with increasing concentrations of VPA, this technique lacks sensitivity to nanoscale structures. Therefore, to quantify intact chromatin structure at the nanoscale level, we took ISOCT measurements on live-cell pellets with or without VPA treatment. From the confocal images of cell nuclei, we could only see a slight shrinkage of chromatin structure at the highest VPA concentration (1.5 mM VPA) in cells treated for 24 h (Fig. 3, *A–D*). Although there is no visual difference from the conventional gray-scale OCT images (Fig. 3, *E–H*), color-coded ISOCT images show significant differences between cells treated with 1.5 mM VPA and controls, as shown in Fig. 3, *I–L*. The change of D values was more obvious in the cores of the pellets, where the cell density was higher than in the superficial layer due to the collection of cells. Specifically, there were higher D values from control CSK cells than from those treated with VPA. D decreased with chromatin decompaction, which is also consistent with the above TEM and confocal image analysis, as shown in Fig. 4 *A*. $B_n(r_d)$ can also be recovered over the sensitive length scale, showing a flatter mass-density autocorrelation function with the chromatin decompaction (i.e., the autocorrelation function decays more slowly at longer spatial length) (Fig. 4 *B*). Fractal changes in the chromatin structure correspond to biological alterations, namely, transcriptional regulation. Compared with conventional microscopy techniques, ISOCT quantifies these fractal changes at subdiffractional length scales down to ~40 nm (28).

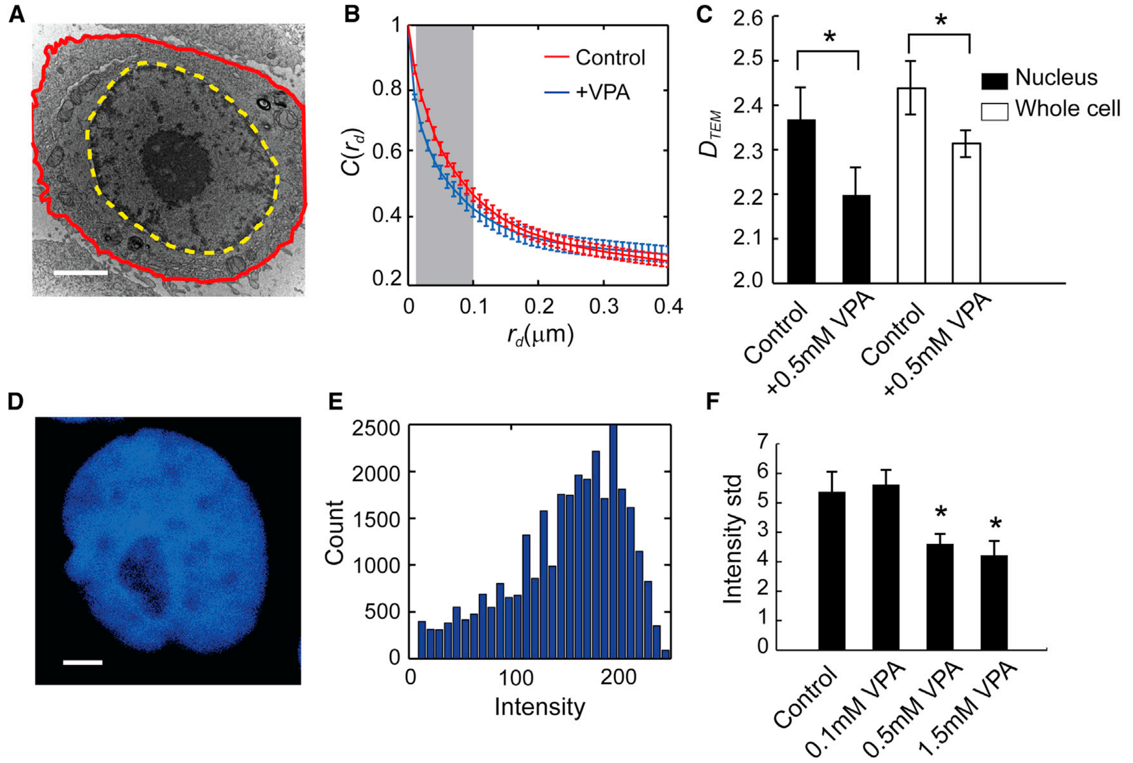

FIGURE 2 Verification of chromatin decompaction. (*A*) A representative image of CSK knockdown cell with nuclear and whole cellular boundary lineated. Scale bar, 2 μm. (*B*) Normalized image correlation function from nuclei ($n = 18$ cells for control, $n = 20$ cells treated). The gray area indicated the range of length scale where the difference between control and treated cells was significant by two sample *t*-tests ($p < 0.05$). Error bars indicate the mean ± SE. (*C*) Fitted D_{TEM} values from $C(r)$ in control and treated cells. (*D*) Magnified image of the nucleus after TOPRO 3 staining by confocal fluorescence microscopy. (*E*) The corresponding fluorescence intensity histogram from (*D*). The intensity standard deviation (*std*) indicates the heterogeneity of the chromatin. (*F*) Intensity standard deviation from cells treated with different concentrations of VPA for 24 h. *$p < 0.05$.

Time course monitor on chromatin decompaction

HDAC inhibitors, including VPA, induce chromatin decompaction but also affect other cellular processes, such as apoptosis. To observe the kinetics of VPA-induced chromatin decompaction, we performed a time-course experiment, as shown in Fig. 4 *C*. Treatment with 0.5 mM VPA showed a progressive decrease of *D* using ISOCT with prolonged treatment. However, this change has no correlation with cell viability, as shown in Fig. 4 *D*, suggesting that the observed trend is caused by the extended effect of VPA on chromatin compaction rather than by cellular apoptosis alone. Furthermore, the time-course study showed that the significant change in *D* happens at ~2–4 h, which conforms with a previous study reporting that the maximum effect of VPA is reached at ~3 h (44). Also, *D* did not change significantly after 4 h treatment, indicating that the effect of VPA has sufficiently taken effect. This also explains why we do not observe dose dependence in Fig. 4 *A* after 24 h treatment.

DISCUSSION

The dysregulation of chromatin compaction is a critical process, particularly in cancers, given the central role of chromatin in cell function. Chromatin alterations can occur at the nucleosomal level (~10 nm) through modifications of the histones, such as by methylation, acetylation, and phosphorylation (45,46). Higher-order structural organization (~30 nm to 1 μm) is regulated through cohesin and condensin protein complexes. Although the importance of chromatin compaction is clearly evident, recent research has attempted to bridge chromatin structure and cellular function using emerging technologies and analysis to characterize the fractality of chromatin compaction (8,15,17). However, it is still challenging to perform such a characterization at subdiffractional length scales in live cells.

Here, we demonstrate, to our knowledge, a novel optical approach, ISOCT, to characterize the fractality of chromatin decompaction in live cells at a length scale from ~30 nm to 450 nm. We adopted a well-established in vitro model using VPA to induce chromatin relaxation. The chromatin decompaction was confirmed by TEM and confocal analysis. Importantly, we found that upon treatment with VPA, cells have a fractal mass density distribution ($D < 3$). We consistently observed a reduced fractal dimension, *D*, upon treatment with VPA at various concentrations, suggesting a sharper mass-density autocorrelation function in the subdiffractional regime. Using the formulism of the WM

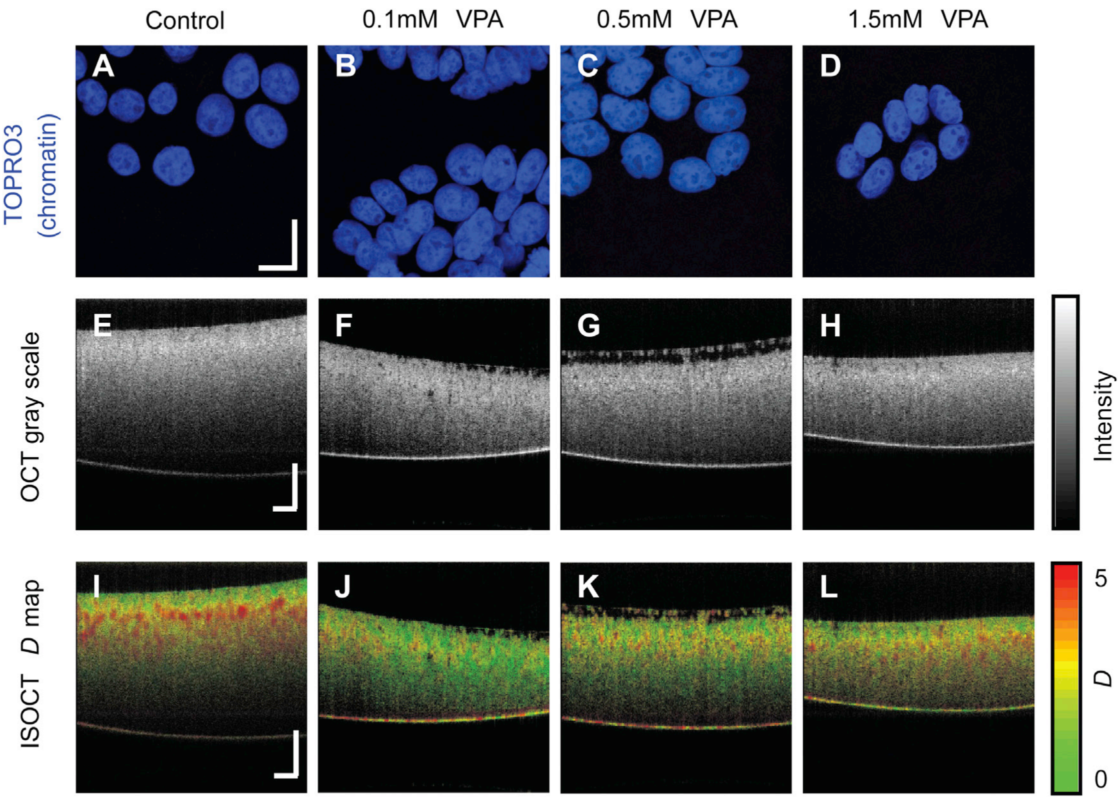

FIGURE 3 Confocal fluorescence, OCT, and ISOCT images of CSK knockdown (CSK−) cells with VPA treatment. (*A–D*) TOPRO3 labels the accessible DNA distribution. (*E–H*) Gray-scale OCT images. (*I–L*) ISOCT images pseudocolored with D. Scale bars, 5 μm in (*A*)–(*H*) and 200 μm in (*E*)–(*L*).

correlation functional family, we have measured and characterized various tissues with D values around 3 where, in some cases, D went above 3 (27,29,30,47,48). In the WM model, the shape of the mass-density correlation function changes from fractal to stretched exponential when $3 < D < 4$. It is worth pointing out that when $D = 3$, the phase function has exactly the same shape as the Henyey-Greenstein (HG) phase function, which has been one of

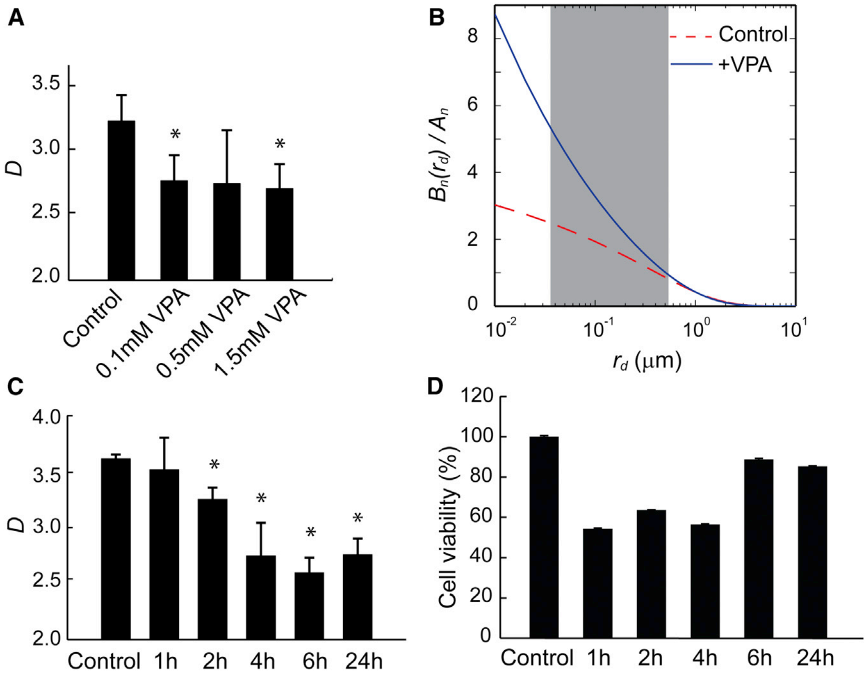

FIGURE 4 (*A*) Bar plots showing ISOCT measurements of D from CSK knockdown cells after 24 h treatment with different concentrations of VPA. (*B*) The recovered $B_n(r_d)$ by the measured D from control cells and those treated with 0.5 mM VPA. The functions were normalized at $r_d = 1$ μm. The gray area shows the length scale of sensitivity of D measurement by ISOCT. (*C*) The progression of D changes after different incubation times with 0.5 mM VPA. (*D*) The corresponding cell viability from cells in (*C*). Error bars indicate the mean ± SE. $^*p < 0.05$. To see this figure in color, go online.

the most popular models in tissue biophotonics (28). Thus, measuring D around 3 is consistent with the convention of using the HG phase function to characterize tissue optical properties.

When characterizing the fractal dimension from biological samples, we should also pay attention to the length-scale range of the measurements. Although the mathematical definition of the power-law function extends over an infinite length scale, in reality, the power-law function is always best fitted within a particular length-scale range. This is best shown in the neutron-scattering study on fixed nuclei by D. V. Lebedev et al., where the fractal dimension was significantly different in two different length scales (17). As summarized in Table 1, neutron scattering and rheology covered the length scale to a subdiffractional range down to 60 nm. TEM studied length scales from 0.01 to 0.4 μm. Hi-C characterized length scales above 0.5 μm. Imaging-based methods and a/LCI measure fractal dimension from ~0.5 μm up to 30 μm. At a similar length scale, our measured value is slightly higher than the values from neutron scattering and rheology, but within a range similar to that of the TEM study (50).

The study has several biological and clinical implications. First, from a biological perspective, HDACs are one of the key enzymes involved in higher-order chromatin remodeling and are directly associated with a broad spectrum of genome functions, such as apoptosis, differentiation, and angiogenesis. The capability of monitoring the HDAC-associated chromatin remodeling at submicron length scales opens opportunities for noninvasive and in situ study of the role of chromatin compaction in the above physiological phenomenon. Second, there are emerging clinical applications of elastic light scatting in cancer detection based on these ultrastructural alterations (51). One of the applications is the detection of field carcinogenesis, the earliest stage of carcinogenesis (52). The concept of field carcinogenesis is that a diffuse injury from genetic/environmental stimuli proceeds and results in local tumorigenesis (53). It has been consistently reported that a higher D is present in field carcinogenesis across different cancer types (colorectal cancer (54), pancreatic cancer (55), and lung cancer (56)), and has been measured by different optical methods (low-coherence enhanced backscattering (55), elastic backscattering spectrometry (47), and ISOCT (30)). Recently, a TEM study showed that chromatin compaction was elevated in colorectal cancer field carcinogenesis, which is associated with overexpression of HDACs (33,50). The study presented here directly demonstrates that higher D could be a result of HDAC overexpression, which implies that chromatin compaction could be a universal marker for field carcinogenesis. Third, given the pivotal role of HDACs in cancer pathology, various HDAC inhibitors have been developed as chemotherapy agents (57). Being able to quantify chromatin remodeling upon HDAC inhibition treatment could serve as an evaluation of drug effectiveness.

The limitation of this study is that we cannot explicitly exclude contributions from the cytoplasm. However, given that the nucleus is the biggest scatterer inside cells and accounts for >50% of cell volume in HT-29 cells (36), the changes that we observed should be reasonably dominated by chromatin decompaction. This is also supported by TEM image analysis showing that the nuclei contributed mostly to the whole-cell D_{TEM} changes (Fig. 2 *C*). Other optical spectroscopic analysis based on higher resolution, such as optical coherence microscopy, could be further deployed to investigate the cell nucleus more specifically.

CONCLUSIONS

Here, we introduce, to our knowledge, a novel optical approach via ISOCT to characterize chromatin decompaction induced by HDAC inhibitors over length scales ranging from 30 nm to 450 nm in live cells (28). A decrease of D was reported when chromatin compaction was relaxed. The method opens the possibility of characterizing higher-order chromatin remodeling at the submicron length scale in live cells in situ.

AUTHOR CONTRIBUTIONS

J.Y. designed the study, performed ISOCT measurements and analyzed the data. Y.S. and C.S.B. prepared the cell specimens. Y.S. performed TEM measurements. J.Y. and Y.S. wrote the article. H.K.R. and V.B. supervised the study.

TABLE 1 Summary of methods for measuring cell nuclear fractal dimension

Method	Fractal Dimension	Length Scale of Measurements (μm)	Sample
Neutron scattering (17,18)	2.2–3.2	0.06–5	isolated nuclei
Hi-C (8)	2.92	0.5–2	DNA fragments
Rheology (21)	2.2–2.6	0.02–2	living cells
a/LCI (22,23)	1.6–2.0	1–30	living cells
Box counting (23,49)	1.6–1.8, 1.2–1.3	0.4–10	fixed and stained cells
Textural analysis (20)	2.8–2.9	0.4–3	fixed cells
TEM (50)	2.6–3.4	0.01–0.4	fixed tissues
ISOCT	2.5–3.6	0.03–0.45	living cells

ACKNOWLEDGMENTS

The authors acknowledge financial support from National Institutes of Health (NIH) grants R01CA165309, R01CA155284, and R01CA173745 and National Science Foundation grant EFRI-1240416.

REFERENCES

1. Lee, Y. W., C. B. Klein, …, M. Costa. 1995. Carcinogenic nickel silences gene expression by chromatin condensation and DNA methylation: a new model for epigenetic carcinogens. *Mol. Cell. Biol.* 15:2547–2557.
2. Francis, N. J., R. E. Kingston, and C. L. Woodcock. 2004. Chromatin compaction by a polycomb group protein complex. *Science.* 306:1574–1577.
3. Donaldson, A. D. 2005. Shaping time: chromatin structure and the DNA replication programme. *Trends Genet.* 21:444–449.
4. Kouzarides, T. 2007. Chromatin modifications and their function. *Cell.* 128:693–705.
5. Felsenfeld, G. 1992. Chromatin as an essential part of the transcriptional mechanism. *Nature.* 355:219–224.
6. Agalioti, T., G. Chen, and D. Thanos. 2002. Deciphering the transcriptional histone acetylation code for a human gene. *Cell.* 111:381–392.
7. Jenuwein, T., and C. D. Allis. 2001. Translating the histone code. *Science.* 293:1074–1080.
8. Lieberman-Aiden, E., N. L. van Berkum, …, J. Dekker. 2009. Comprehensive mapping of long-range interactions reveals folding principles of the human genome. *Science.* 326:289–293.
9. O'Brien, T. P., C. J. Bult, …, R. van Driel. 2003. Genome function and nuclear architecture: from gene expression to nanoscience. *Genome Res.* 13 (6A):1029–1041.
10. Maeshima, K., S. Hihara, and M. Eltsov. 2010. Chromatin structure: does the 30-nm fibre exist in vivo? *Curr. Opin. Cell Biol.* 22:291–297.
11. Nishino, Y., M. Eltsov, …, K. Maeshima. 2012. Human mitotic chromosomes consist predominantly of irregularly folded nucleosome fibres without a 30-nm chromatin structure. *EMBO J.* 31:1644–1653.
12. Fussner, E., R. W. Ching, and D. P. Bazett-Jones. 2011. Living without 30 nm chromatin fibers. *Trends Biochem. Sci.* 36:1–6.
13. Fussner, E., M. Strauss, …, D. P. Bazett-Jones. 2012. Open and closed domains in the mouse genome are configured as 10-nm chromatin fibres. *EMBO Rep.* 13:992–996.
14. Ricci, M. A., C. Manzo, …, M. P. Cosma. 2015. Chromatin fibers are formed by heterogeneous groups of nucleosomes in vivo. *Cell.* 160:1145–1158.
15. Bancaud, A., C. Lavelle, …, J. Ellenberg. 2012. A fractal model for nuclear organization: current evidence and biological implications. *Nucleic Acids Res.* 40:8783–8792.
16. Metze, K. 2010. Fractal dimension of chromatin and cancer prognosis. *Epigenomics.* 2:601–604.
17. Lebedev, D. V., M. V. Filatov, …, V. V. Isaev-Ivanov. 2005. Fractal nature of chromatin organization in interphase chicken erythrocyte nuclei: DNA structure exhibits biphasic fractal properties. *FEBS Lett.* 579:1465–1468.
18. Lebedev, D. V., M. V. Filatov, …, V. V. Isaev-Ivanov. 2008. Structural hierarchy of chromatin in chicken erythrocyte nuclei based on small-angle neutron scattering: fractal nature of the large-scale chromatin organization. *Crystallogr. Rep.* 53:110–115.
19. Mateos-Langerak, J., M. Bohn, …, S. Goetze. 2009. Spatially confined folding of chromatin in the interphase nucleus. *Proc. Natl. Acad. Sci. USA.* 106:3812–3817.
20. Einstein, A. J., H. S. Wu, and J. Gil. 1998. Fractal characterization of nuclear texture in breast cytology: frequency and spatial domain approaches. *In* Fractals in Biology and Medicine. G. Losa, D. Merlini, T. Nonnenmacher, and E. Weibel, editors. Birkhäuser, Basel, Switzerland, pp. 190–206.
21. Bancaud, A., S. Huet, …, J. Ellenberg. 2009. Molecular crowding affects diffusion and binding of nuclear proteins in heterochromatin and reveals the fractal organization of chromatin. *EMBO J.* 28:3785–3798.
22. Wax, A., C. Yang, …, M. S. Feld. 2002. Cellular organization and substructure measured using angle-resolved low-coherence interferometry. *Biophys. J.* 82:2256–2264.
23. Chalut, K. J., J. H. Ostrander, …, A. Wax. 2009. Light scattering measurements of subcellular structure provide noninvasive early detection of chemotherapy-induced apoptosis. *Cancer Res.* 69:1199–1204.
24. Rogers, J. D., A. J. Radosevich, …, V. Backman. 2014. Modeling light scattering in tissue as continuous random media using a versatile refractive index correlation function. selected topics in quantum electronics. *IEEE J. Sel. Top. Quantum Electron.* 20:173–186.
25. Boustany, N. N., S. A. Boppart, and V. Backman. 2010. Microscopic imaging and spectroscopy with scattered light. *Annu. Rev. Biomed. Eng.* 12:285–314.
26. Hunter, M., V. Backman, …, M. S. Feld. 2006. Tissue self-affinity and polarized light scattering in the born approximation: a new model for precancer detection. *Phys. Rev. Lett.* 97:138102.
27. Cherkezyan, L., I. Capoglu, …, V. Backman. 2013. Interferometric spectroscopy of scattered light can quantify the statistics of subdiffractional refractive-index fluctuations. *Phys. Rev. Lett.* 111:033903.
28. Yi, J., A. J. Radosevich, …, V. Backman. 2013. Can OCT be sensitive to nanoscale structural alterations in biological tissue? *Opt. Express.* 21:9043–9059.
29. Yi, J., and V. Backman. 2012. Imaging a full set of optical scattering properties of biological tissue by inverse spectroscopic optical coherence tomography. *Opt. Lett.* 37:4443–4445.
30. Yi, J., A. J. Radosevich, …, V. Backman. 2014. Spatially resolved optical and ultrastructural properties of colorectal and pancreatic field carcinogenesis observed by inverse spectroscopic optical coherence tomography. *J. Biomed. Opt.* 19:36013.
31. Barer, R., and S. Tkaczyk. 1954. Refractive index of concentrated protein solutions. *Nature.* 173:821–822.
32. Davies, H. G., M. H. F. Wilkins, …, L. F. La Cour. 1954. The use of the interference microscope to determine dry mass in living cells and as a quantitative cytochemical method. *Q. J. Microsc. Sci.* s3–95:271–304.
33. Stypula-Cyrus, Y., D. Damania, …, V. Backman. 2013. HDAC up-regulation in early colon field carcinogenesis is involved in cell tumorigenicity through regulation of chromatin structure. *PLoS One.* 8:e64600.
34. Marchion, D. C., E. Bicaku, …, P. N. Munster. 2005. Valproic acid alters chromatin structure by regulation of chromatin modulation proteins. *Cancer Res.* 65:3815–3822.
35. Kunte, D. P., R. K. Wali, …, H. K. Roy. 2005. Down-regulation of the tumor suppressor gene C-terminal Src kinase: an early event during premalignant colonic epithelial hyperproliferation. *FEBS Lett.* 579:3497–3502.
36. Damania, D., H. Subramanian, …, V. Backman. 2010. Role of cytoskeleton in controlling the disorder strength of cellular nanoscale architecture. *Biophys. J.* 99:989–996.
37. Kunte, D. P., R. K. Wali, …, H. K. Roy. 2008. Antiproliferative effect of sulindac in colonic neoplasia prevention: role of COOH-terminal Src kinase. *Mol. Cancer Ther.* 7:1797–1806.
38. Subramanian, H., P. Pradhan, …, V. Backman. 2008. Optical methodology for detecting histologically unapparent nanoscale consequences of genetic alterations in biological cells. *Proc. Natl. Acad. Sci. USA.* 105:20118–20123.
39. Krämer, O. H., P. Zhu, …, M. Göttlicher. 2003. The histone deacetylase inhibitor valproic acid selectively induces proteasomal degradation of HDAC2. *EMBO J.* 22:3411–3420.
40. Schmitt, J. M., and G. Kumar. 1996. Turbulent nature of refractive-index variations in biological tissue. *Opt. Lett.* 21:1310–1312.
41. Sheppard, C. J. R. 2007. Fractal model of light scattering in biological tissue and cells. *Opt. Lett.* 32:142–144.

42. Xu, M., and R. R. Alfano. 2005. Fractal mechanisms of light scattering in biological tissue and cells. *Opt. Lett.* 30:3051–3053.
43. Rogers, J. D., İ. R. Capoğlu, and V. Backman. 2009. Nonscalar elastic light scattering from continuous random media in the Born approximation. *Opt. Lett.* 34:1891–1893.
44. Tung, E. W. Y., and L. M. Winn. 2010. Epigenetic modifications in valproic acid-induced teratogenesis. *Toxicol. Appl. Pharmacol.* 248:201–209.
45. Sawan, C., and Z. Herceg. 2010. Histone modifications and cancer. *Adv. Genet.* 70:57–85.
46. Zentner, G. E., and S. Henikoff. 2013. Regulation of nucleosome dynamics by histone modifications. *Nat. Struct. Mol. Biol.* 20:259–266.
47. Radosevich, A. J., N. N. Mutyal, …, V. Backman. 2013. Ultrastructural alterations in field carcinogenesis measured by enhanced backscattering spectroscopy. *J. Biomed. Opt.* 18:097002.
48. Mutyal, N. N., A. J. Radosevich, …, V. Backman. 2015. In vivo risk analysis of pancreatic cancer through optical characterization of duodenal mucosa. *Pancreas.* 44:735–741.
49. Goutzanis, L., N. Papadogeorgakis, …, C. Alexandridis. 2008. Nuclear fractal dimension as a prognostic factor in oral squamous cell carcinoma. *Oral Oncol.* 44:345–353.
50. Cherkezyan, L., Y. Stypula-Cyrus, …, V. Backman. 2014. Nanoscale changes in chromatin organization represent the initial steps of tumorigenesis: a transmission electron microscopy study. *BMC Cancer.* 14:189.
51. Boppart, S. A., and R. Richards-Kortum. 2014. Point-of-care and point-of-procedure optical imaging technologies for primary care and global health. *Sci. Transl. Med.* 6:253rv2.
52. Backman, V., and H. K. Roy. 2013. Advances in biophotonics detection of field carcinogenesis for colon cancer risk stratification. *J. Cancer.* 4:251–261.
53. Chai, H., and R. E. Brown. 2009. Field effect in cancer-an update. *Ann. Clin. Lab. Sci.* 39:331–337.
54. Roy, H. K., V. Turzhitsky, …, V. Backman. 2009. Association between rectal optical signatures and colonic neoplasia: potential applications for screening. *Cancer Res.* 69:4476–4483.
55. Turzhitsky, V., Y. Liu, …, R. Brand. 2008. Investigating population risk factors of pancreatic cancer by evaluation of optical markers in the duodenal mucosa. *Dis. Markers.* 25:313–321.
56. Radosevich, A. J., N. N. Mutyal, …, H. K. Roy. 2014. Buccal spectral markers for lung cancer risk stratification. *PLoS One.* 9:e110157.
57. Rodriquez, M., M. Aquino, …, L. Gomez-Paloma. 2006. Chemistry and biology of chromatin remodeling agents: state of art and future perspectives of HDAC inhibitors. *Curr. Med. Chem.* 13:1119–1139.